Water Splitting

DOI: 10.1002/anie.201408441

Perovskite Oxide Nanosheets with Tunable Band-Edge Potentials and High Photocatalytic Hydrogen-Evolution Activity**

Kazuhiko Maeda, Miharu Eguchi, and Takayoshi Oshima*

Abstract: *Perovskite nanosheets of $HCa_{2-x}Sr_xNb_3O_{10}$ and $HCa_2Nb_{3-y}Ta_yO_{10}$ with controlled band-edge potentials were prepared. They worked as highly efficient heterogeneous photocatalysts for H_2 evolution from a water/methanol mixture under band-gap irradiation. The activity was found to depend on the composition. The highest activity was obtained with $HCa_2Nb_2TaO_{10}$ nanosheets, recording an apparent quantum yield of approximately 80 % at 300 nm, which is the highest value for a nanosheet-based photocatalyst reported to date.*

Certain layered compounds, such as metal oxides,[1] hydroxides,[2] sulfides[3] and nitrides,[4] undergo exfoliation to yield unilamellar colloids by reaction with a suitable guest molecule. The produced colloids are two-dimensional nanocrystals, so-called "nanosheets", with a thickness of approximately 1 nm and lateral dimensions ranging from several hundred nanometers to a few micrometers. Nanosheets having anisotropic features have attracted considerable attention as functional materials including optoelectronics,[5] and heterogeneous photocatalysis.[6–10] The material's functionality including (photo)catalytic activity is affected strongly by the structural features. Several researchers have reported the superior photocatalytic functionality of nanosheet materials to the corresponding lamellar solids.[6a,7c,9d] Very recently, CuO nanoplates having exposed {001} facets have been shown to exhibit an enhanced catalytic activity for NO gas removal.[11]

In addition to such structural aspects, a certain function (e.g., photocatalytic property) of a given metal oxide depends on its elemental composition, as it determines the physicochemical properties of the material.[12] For application in photocatalysis the composition of a metal oxide determines the band structure of the material, which has a strong impact on the photocatalytic activity, as the reactivity of electrons and holes for surface redox reactions is determined by the band-edge potentials.[12] Therefore, precise control of the energy band structure is essential to designing a highly efficient photocatalyst. To date, however, it should be stressed that such band-structure-controlled nanosheets have not been devised, and how the band-gap structure affects photocatalytic activity remains little explored. The lack of such information limits further development of a highly active photocatalysts based on nanosheets.

Among metal oxide nanosheets reported to date, $Ca_2Nb_3O_{10}^-$ nanosheet with 1.6 ± 0.2 nm thickness (based on AFM observations),[5,10b] classified with Dion–Jacobson type perovskite,[1a] is one of the most studied ones not only as a photocatalyst[6–10] but as another functional material.[13,14] Ebina et al. have reported photocatalytic activities of aggregated $HCa_2Nb_3O_{10}$ nanosheets for H_2 evolution from an aqueous methanol solution and overall water splitting under ultraviolet (UV) light irradiation (>200 nm).[6] Osterloh et al. have revealed photocatalytic activity of individual $Ca_2Nb_3O_{10}^-$ nanosheets for H_2 evolution.[7] They also found that this material is capable of producing H_2 and hydrogen peroxide from pure water under band-gap irradiation.[8] Our group has studied the same material both as a building block for dye-sensitized H_2 evolution with visible light[9a,b] and as a UV-light-driven photocatalyst for water splitting.[9b–d] Ida et al. have investigated doping effects of Rh ions into the lattice of $Ca_2Nb_3O_{10}^-$ nanosheets for H_2 evolution.[10a]

Perovskite-type metal oxides, generally expressed as ABO_3, consist of corner-shared BO_6 octahedra stacking to form a three-dimensional crystal and A cations locating in the 12-coordination environment. In perovskite type metal oxide semiconductors, changing the A site cations modulates distortion of B-O-B bonding angle, which is ideally 180°, depending on exchanged cations. The distortion of the bonding angle greatly affects physicochemical properties of the material, which include the conduction-band potential and the band-gap energy.[15] While such "band-engineering" has often been applied to bulk-type semiconductor materials of not only metal oxides but also sulfides,[12a] however, no one has reported how effective it is for oxide nanosheets. Applying the band-engineering strategy to oxide nanosheets will give us useful information for further development of photocatalytic systems based on nanosheets.

In this study, we prepared band-edge tunable perovskite nanosheets of $HCa_{2-x}Sr_xNb_3O_{10}$ and $HCa_2Nb_{3-y}Ta_yO_{10}$, which worked as highly efficient photocatalysts for H_2 evolution

[*] Prof. Dr. K. Maeda, T. Oshima
Department of Chemistry, Graduate School of Science and Engineering, Tokyo Institute of Technology
2-12-1-NE-2 Ookayama, Meguro-ku, Tokyo 152-8550 (Japan)
E-mail: maedak@chem.titech.ac.jp
Dr. M. Eguchi
Department of Chemistry, Graduate School of Pure and Applied Sciences, University of Tsukuba
1-1-1 Tennodai, Tsukuba, Ibaraki 305-8571 (Japan)
and
Precursory Research for Embryonic Science and Technology (Japan) Science and Technology Agency
4-1-8 Honcho, Kawaguchi, Saitama 332-0012 (Japan)

[**] We thank Ryouhei Noma, Prof. Kiyotaka Nakajima, and Prof. Michikazu Hara (Tokyo Institute of Technology) for assistance in Raman measurements. This work was supported by the ENEOS Hydrogen Trust Fund, Grant-in-Aid for Scientific Research on Innovative Areas (Project No. 25107512; AnApple), and the PRESTO/JST program "Chemical Conversion of Light Energy".

Supporting information for this article is available on the WWW under http://dx.doi.org/10.1002/anie.201408441.

under band-gap irradiation, giving apparent quantum yields (AQYs) of approximately 80% at 300 nm. The maximum AQY is the highest value among nanosheet-based photocatalysts reported to date.

The detail of materials preparation is included in Supporting Information where Figure S1 shows X-ray diffraction (XRD) patterns of layered $KCa_{2-x}Sr_xNb_3O_{10}$ materials. The samples of $x=0$ and 2 show the single-phase diffraction pattern assigned to layered $KCa_2Nb_3O_{10}$ and $KSr_2Nb_3O_{10}$, respectively. The shape of the diffraction pattern undergoes a change from that of $KCa_2Nb_3O_{10}$ to $KSr_2Nb_3O_{10}$ as the Sr content in $KCa_{2-x}Sr_xNb_3O_{10}$ increases, suggesting the successful substation of Ca for Sr. Lamellar solids of $KCa_2Nb_{3-y}Ta_yO_{10}$ ($y \leq 1.5$) were also prepared in a similar manner. Figure S1 also shows that single-phase diffraction patterns assigned to $KCa_2Nb_3O_{10}$ are observed up to $y=1.5$, suggestive of successful preparation of $KCa_2Nb_{3-y}Ta_yO_{10}$. However, it was difficult to synthesize $KCa_2Nb_{3-y}Ta_yO_{10}$ with $y>1.5$.

After treating the layered solids with HNO_3 to exchange interlayer K^+ ions with protons, exfoliation was conducted using tetra(*n*-butyl)ammonium hydroxide (TBA^+OH^-). Figure 1 shows TEM images of exfoliated $TBA_zH_{1-z}Ca_{2-x}Sr_xNb_3O_{10}$ and $TBA_zH_{1-z}Ca_2Nb_{3-y}Ta_yO_{10}$ nanosheets derived from lamellar $HCa_{2-x}Sr_xNb_3O_{10}$ and $HCa_2Nb_{3-y}Ta_yO_{10}$ solids. The lateral dimensions of the nanosheets are approximately 500 nm, regardless of the compositional parameters (x and y) although some fragmental, smaller nanosheets are also observable. It indicates that substitution of Ca and Nb in $HCa_2Nb_3O_{10}$ nanosheets for Sr and Ta has little influence on the lateral dimensions.

The colloidal nanosheets were then precipitated by adding HCl to yield restacked $HCa_{2-x}Sr_xNb_3O_{10}$ and $HCa_2Nb_{3-y}Ta_yO_{10}$ nanosheets for use as photocatalysts. Figure S2 shows XRD patterns of restacked $HCa_{2-x}Sr_xNb_3O_{10}$ and $HCa_2Nb_{3-y}Ta_yO_{10}$ nanosheets, along with the data for lamellar $HSr_2Nb_3O_{10}$ for comparison. The XRD pattern of the restacked $HSr_2Nb_3O_{10}$ nanosheet exhibits broader and weaker (001) diffraction peaks, which are shifted to lower angle than the corresponding (002) peak in layered lamellar $HSr_2Nb_3O_{10}$ owing to turbostratic stacking and more hydration. This is supported by the result of SEM observations, which showed that the materials thus obtained consisted of aggregated solids with a disordered structure, regardless of the composition (Figure S3). A significant reduction of the (00l) ($l \geq 2$) peak intensity, compared to the parent solid, indicates a much less-ordered lamellar structure in the restacked materials. Relatively intense (020) and (220) diffraction peaks, arising from in-plane lattice directions, are preserved but broadened. The (*hkl*) reflections are weak and more substantially broadened. This feature indicates that the in-plane crystallinity of the $Sr_2Nb_3O_{10}^-$ nanosheets is preserved after the exfoliation–restacking process to a certain extent. This trend was observed for all of the prepared materials (data not shown). Similar to the corresponding $HCa_2Nb_3O_{10}$ and $HSr_2Nb_3O_{10}$ nanosheet samples (Figure S2), a successive change with respect to the composition was observed in $HCa_{2-x}Sr_xNb_3O_{10}$ samples, suggesting that the prepared materials are solid solutions between $HCa_2Nb_3O_{10}$ and $HSr_2Nb_3O_{10}$. For the Ta substituents of $HCa_2Nb_{3-y}Ta_yO_{10}$, similar successive change was observed with increasing the Ta content. As listed in Table 1, the specific surface areas of the restacked $HCa_{2-x}Sr_xNb_3O_{10}$ nanosheets were 47–65 m^2g^{-1}, and there was no noticeable trend between the surface area and the composition. Nevertheless, these values are much higher than those of the parent solid materials that have typically around 1 m^2g^{-1} specific surface areas. Specific surface areas of $HCa_2Nb_{3-y}Ta_yO_{10}$ nanosheet aggregates tended to decrease with increasing Ta content, and were determined to be 30–50 m^2g^{-1}, smaller than those of $HCa_{2-x}Sr_xNb_3O_{10}$.

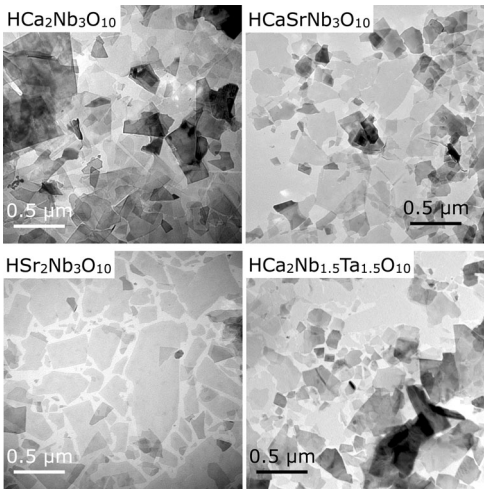

Figure 1. Typical TEM images of TBA^+-exfoliated $Ca_{2-x}Sr_xNb_3O_{10}^-$ and $Ca_2Nb_{3-y}Ta_yO_{10}^-$ nanosheets.

Table 1: Specific surface areas, atomic compositions, and photocatalytic activities of restacked $HCa_{2-x}Sr_xNb_3O_{10}$ and $HCa_2Nb_{3-y}Ta_yO_{10}$ nanosheets.

Entry	Ideal composition	Specific surface area [m^2g^{-1}]	Atomic composition[a] [mol%]					Apparent quantum yield at 300 nm[b] [%]
			K	Ca	Sr	Nb	Ta	
1	$HCa_2Nb_3O_{10}$	48	0.3	41.5	0	58.2	0	51±4
2	$HCa_{1.5}Sr_{0.5}Nb_3O_{10}$	47	0.3	30.3	9.1	60.3	0	48±3
3	$HCaSrNb_3O_{10}$	58	0.4	19.6	18.4	61.6	0	44±5
4	$HCa_{0.5}Sr_{1.5}Nb_3O_{10}$	50	0.5	8.8	29.0	61.7	0	39±1
5	$HSr_2Nb_3O_{10}$	65	0.4	0	38.3	61.3	0	39±3
6	$HCa_2Nb_{2.7}Ta_{0.3}O_{10}$	48	1.2	40.6	0	53.3	4.9	71±5
7	$HCa_2Nb_2TaO_{10}$	39	0.6	39.1	0	40.0	20.1	78±2
8	$HCa_2Nb_{1.5}Ta_{1.5}O_{10}$	29	0.5	39.5	0	31.1	28.9	65±7

[a] Measured by EDX. [b] Reaction conditions: catalyst, 25 mg (0.5 wt% Pt-loaded); aqueous solution containing 10 vol.% methanol (100 mL); light source: xenon lamp (300 W) with a band-pass filter. The corresponding H_2 evolution rates are summarized in Table S1 (Supporting Information).

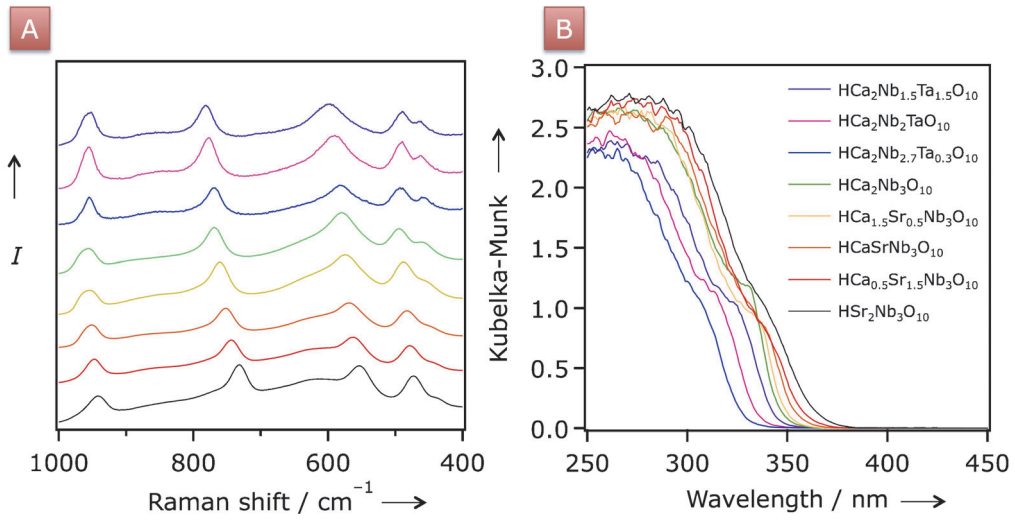

Figure 2. A) Raman spectra and B) UV/Vis diffuse reflectance spectra of restacked $HCa_{2-x}Sr_xNb_3O_{10}$ and $HCa_2Nb_{3-y}Ta_yO_{10}$ nanosheets.

Raman spectroscopy is a powerful technique that allows the local structure of solid materials to be examined. Figure 2 A shows Raman spectra of the restacked $HCa_{2-x}Sr_xNb_3O_{10}$ and $HCa_2Nb_{3-y}Ta_yO_{10}$ nanosheets. All of the samples gave Raman bands at around 960–940, 780–730, 600–550, and 500–450 cm^{-1}. The assignment of the Raman bands is possible according to previous work on the corresponding layered materials.[16] The spectral shapes of the $HCa_2Nb_3O_{10}$ and $HSr_2Nb_3O_{10}$ nanosheets are similar to each other. With increasing the Sr content (x), however, the positions of the Raman bands in $HCa_{2-x}Sr_xNb_3O_{10}$ shifted to lower wavenumbers, indicating the bond length becomes longer. Although the crystal structure of $HSr_2Nb_3O_{10}$ (or $KSr_2Nb_3O_{10}$) has not been reported in detail to date, substitution of Ca^{2+} ions having ionic radius of 0.148 nm in the 12-coordination environment for the larger Sr^{2+} ions (0.158 nm)[16] is likely to expand the perovskite layers and relax the lattice distortion, resulting in the red shift of the Raman bands. A similar red shift in the Raman bands has been observed for layered $CsA_2Nb_3O_{10}$ (A = Ca, Sr, and Ba).[16b] This successive shift further supports the formation of solid solution between $HCa_2Nb_3O_{10}$ and $HSr_2Nb_3O_{10}$.

For $HCa_2Nb_{3-y}Ta_yO_{10}$ materials, a similar peak shift can be seen. Raman bands appearing at around 750 and 570 cm^{-1}, which are, respectively, assigned to weakly distorted central MO_6 octahedra and highly distorted external MO_6 in the triple perovskite block, shift to higher wavenumbers with increasing the Ta content, indicating more pronounced distortion (or shrinkage) of the triple perovskite layers. However, the positions of the 960 cm^{-1} band, which originates from the symmetric stretching mode of M–O terminal bond, remained unchanged even upon Ta substitution, different from $HCa_{2-x}Sr_xNb_3O_{10}$ analogues.

Although the difference in ionic radius between Ta^{5+} and Nb^{5+} in 6-coordination environment is negligibly small,[17] the substitution of Nb^{5+} in $HCa_2Nb_3O_{10}$ for Ta^{5+} was found to result in pronounced distortion of the triple perovskite layers that consist of MO_6 octahedra. However, the degree of distortion that results from the Ta substitution differs with respect to each Raman mode, as the 495 cm^{-1} band assignable to the external MO_6 octahedrons does not undergo a change upon Ta substitution. Thus, Raman measurements can distinguish the local structure of the restacked $HCa_{2-x}Sr_xNb_3O_{10}$ and $HCa_2Nb_{3-y}Ta_yO_{10}$ nanosheets, which is difficult to resolve by XRD.

Table 1 lists atomic compositions of the same restacked nanosheets, which were measured by energy dispersive X-ray (EDX) spectroscopy. Although the measured atomic compositions are slightly deviated from those expected from the ideal compositions, the data clearly indicates successful substitution of Ca and Nb for Sr and Ta in the entire compositional range examined. Note that in all cases, a small amount of residual K was detected. This means that complete exchange of interlayer K^+ ions with protons is difficult owing to the limited access of protons inside the interlayer space.

The gradual change in the atomic composition of the nanosheets was expected to affect the optical light absorption properties of the materials. Figure 2 B shows UV/Vis diffuse reflectance spectra (DRS) for the same restacked samples. All samples exhibit absorption bands at around 330–370 nm. The position of the absorption edge of $HCa_{2-x}Sr_xNb_3O_{10}$ shifts to longer wavelengths with increasing the Sr content. The band-gap energy decreased from 3.59 (for $x = 0$) to 3.40 eV (for $x = 2$), which was estimated from the onset wavelength of DRS. The band-gap decrease is due to the bond angle of Nb-O-Nb being closer to 180°, as the Sr content increases.[12] As indicated by Raman spectroscopy (Figure 2 A), the NbO_6 octahedra in the perovskite blocks of $HCa_{2-x}Sr_xNb_3O_{10}$ become less distorted as the concentration of Sr increases. This leads to greater delocalization of the excited state energy and decreasing band-gap energy.[15]

According to the report by Scaife,[18] the valence band of metal oxides containing d^0-early transition metal cations (e.g., Nb^{5+} and Ta^{5+}) is composed of oxygen 2p orbitals, which are located at around 3 V versus the normal hydrogen electrode (NHE; at pH 0), regardless of the composition. Therefore, the difference in band-gap energy of $HCa_{2-x}Sr_xNb_3O_{10}$ could originate from that in the conduction-band potential. More specifically, the conduction-band potential of $HCa_{2-x}Sr_xNb_3O_{10}$ nanosheets shifts positively with increasing the Sr content.

On the other hand, increasing the Ta content in $HCa_2Nb_{3-y}Ta_yO_{10}$ resulted in a blue-shift of the absorption edge. Metal oxides containing Ta^{5+} ions as the principal cationic component have a more negative conduction-band

potential than those containing principally Nb^{5+}.[12] The observed blue-shift can therefore be explained in terms of the conduction-band potential. These results clearly demonstrate that perovskite nanosheets which have controlled optical light absorption properties can be obtained by changing the composition.

On the basis of the characterization shown above, it is reasonably concluded that band-edge tunable nanosheets of $HCa_{2-x}Sr_xNb_3O_{10}$ and $HCa_2Nb_{3-y}Ta_yO_{10}$ are successfully prepared for the first time. Using these nanosheet materials as heterogeneous photocatalysts, H_2 evolution reactions were then conducted under monochromatic light irradiation. As listed in Table 1, it was found that the AQYs of H_2 evolution on these materials were very high, giving 40–80% at 300 nm. The performance tends to decrease with increasing the Sr content, presumably owing to a decrease in the driving force of conduction-band electrons for proton reduction. On the other hand, increasing the Ta content in $HCa_2Nb_{3-y}Ta_yO_{10}$ enhanced the activity up to $y = 1$, then decreasing slightly. The rise of the conduction band potential in $HCa_2Nb_{3-y}Ta_yO_{10}$ with increasing the Ta content appears to be favorable for the reduction of protons to give H_2. At the same time, however, this would lead to inferior light-harvesting (Figure 2B), which contributes to slower H_2 evolution.

The most active sample, $HCa_2Nb_2TaO_{10}$, generated H_2 without noticeable degradation, as shown in Figure S4, giving a maximum AQY of 80%. It should be noted that the performance was higher than that of P25 titania, which is one of the most active non-layered photocatalysts and gave an AQY of 63% under the same reaction condition. Ida et al. have recently reported that a Rh-doped $HCa_2Nb_3O_{10}$ nanosheet exhibited H_2 evolution activity from an aqueous methanol solution, with an AQY of 65%.[10a] The performance of the $HCa_2Nb_2TaO_{10}$ nanosheet was higher than that of the Rh-doped analogue. To our knowledge, the approximately 80% AQY recorded for the $HCa_2Nb_2TaO_{10}$ nanosheet is the highest value for nanosheet-based photocatalysts reported to date. Photocatalytic reactions on an illuminated semiconductor are accomplished when photogenerated electrons and holes move to the surface without recombination, reducing and oxidizing surface-adsorbed species.[12] The nanosized thickness and high surface area of perovskite oxide nanosheets (Figure 1 and Figure S3) are both beneficial in terms of prompt migration of the photogenerated charge carriers to the surface. In addition to this structural effect, the precise control of conduction-band-edge potential that maximizes the reactivity of the conduction-band electrons should be responsible for the high photocatalytic activity of $HCa_2Nb_2TaO_{10}$.

In conclusion, we successfully synthesized for the first time perovskite nanosheets of $HCa_{2-x}Sr_xNb_3O_{10}$ and $HCa_2Nb_{3-y}Ta_yO_{10}$ with tunable band-edge potentials, which exhibited very high photocatalytic activity for H_2 evolution from water. Owing to the unique structural properties, such as high surface area, anisotropic features, and single-crystalline texture, semiconductor nanosheets are attractive building blocks for preparing a multi-component photofunctional materials that incorporate electron donors/acceptors, light-harvesting molecules, and catalytic nanoparticles.[19] The band-edge tunable nanosheets prepared in this study would merit a wide range of photofunctional applications, as the band-edge potential is one of the most important parameters in such applications. Besides, the $HCa_2Nb_2TaO_{10}$ nanosheet that achieves a very high AQY for H_2 evolution may be a promising host material for producing a visible-light-responsive photocatalyst based on metal-ion-doping.[12a] This possibility is currently under investigation in our laboratory.

Received: August 21, 2014
Published online: September 26, 2014

Keywords: heterogeneous photocatalysis · layered compounds · nanosheets · perovskites · water splitting

[1] a) M. M. J. Treacy, S. B. Rice, A. J. Jacobson, J. T. Lewandowski, *Chem. Mater.* **1990**, *2*, 279–286; b) S. W. Keller, H.-N. Kim, T. E. Mallouk, *J. Am. Chem. Soc.* **1994**, *116*, 8817–8818; c) T. Sasaki, M. Watanabe, H. Hashizume, H. Yamada, H. Nakazawa, *J. Am. Chem. Soc.* **1996**, *118*, 8329–8335.

[2] a) M. Adachi-Pagano, C. Forano, J.-P. Besse, *Chem. Commun.* **2000**, 91–92; b) F. Leroux, M. Adachi-Pagano, M. Intissar, S. Chauvière, C. Forano, J.-P. Besse, *J. Mater. Chem.* **2001**, *11*, 105–112; c) R. Ma, K. Takada, K. Fukuda, N. Iyi, Y. Bando, T. Sasaki, *Angew. Chem. Int. Ed.* **2008**, *47*, 86–89; *Angew. Chem.* **2008**, *120*, 92–95; d) S. Ida, D. Shiga, M. Koinuma, Y. Matsumoto, *J. Am. Chem. Soc.* **2008**, *130*, 14038–14039.

[3] a) P. Joensen, R. F. Frindt, S. R. Morrison, *Mater. Res. Bull.* **1986**, *21*, 457–461; b) D. Yang, S. Jiménez Sandoval, W. M. R. Divigalpitiya, J. C. Irwin, R. F. Frindt, *Phys. Rev. B* **1991**, *43*, 12053.

[4] a) P. Niu, L. Zhang, G. Liu, H. M. Cheng, *Adv. Funct. Mater.* **2012**, *22*, 4763–4770; b) Z. Lin, X. Wang, *Angew. Chem. Int. Ed.* **2013**, *52*, 1735–1738; *Angew. Chem.* **2013**, *125*, 1779–1782.

[5] M. Osada, T. Sasaki, *Adv. Mater.* **2012**, *24*, 210–228.

[6] a) Y. Ebina, T. Sasaki, M. Harada, M. Watanabe, *Chem. Mater.* **2002**, *14*, 4390–4395; b) Y. Ebina, N. Sakai, T. Sasaki, *J. Phys. Chem. B* **2005**, *109*, 17212–17216.

[7] a) O. C. Compton, E. C. Carroll, J. Y. Kim, D. S. Larsen, F. E. Osterloh, *J. Phys. Chem. C* **2007**, *111*, 14589–14592; b) E. M. Sabio, R. L. Chamousis, N. D. Browning, F. E. Osterloh, *J. Phys. Chem. C* **2008**, *116*, 3161–3170; c) E. M. Sabio, R. L. Chamousis, N. D. Browning, F. E. Osterloh, *J. Phys. Chem. C* **2012**, *116*, 3161–3170.

[8] O. C. Compton, F. E. Osterloh, *J. Phys. Chem. C* **2009**, *113*, 479–485.

[9] a) K. Maeda, M. Eguchi, S.-H. A. Lee, W. J. Youngblood, H. Hata, T. E. Mallouk, *J. Phys. Chem. C* **2009**, *113*, 7962–7969; b) K. Maeda, M. Eguchi, W. J. Youngblood, T. E. Mallouk, *Chem. Mater.* **2009**, *21*, 3611–3617; c) K. Maeda, T. E. Mallouk, *J. Mater. Chem.* **2009**, *19*, 4813–4818; d) T. Oshima, O. Ishitani, K. Maeda, *Adv. Mater. Interfaces* **2014**, DOI: 10.1002/admi.201400131.

[10] a) Y. Okamoto, S. Ida, J. Hyodo, H. Hagiwara, T. Ishihara, *J. Am. Chem. Soc.* **2011**, *133*, 18034–18037; b) S. Ida, A. Takashiba, S. Koga, H. Hagiwara, T. Ishihara, *J. Am. Chem. Soc.* **2014**, *136*, 1872–1878.

[11] F. M. Auxilia, S. Ishihara, S. Mandal, T. Tanabe, G. Saravanan, G. V. Ramesh, N. Umezawa, T. Hara, Y. Xu, S. Hishita, Y. Yamauchi, A. Dakshanamoorthy, J. P. Hill, K. Ariga, H. Abe, *Adv. Mater.* **2014**, *26*, 4481–4485.

[12] a) A. Kudo, Y. Miseki, *Chem. Soc. Rev.* **2009**, *38*, 253–278; b) K. Maeda, *J. Photochem. Photobiol. C* **2011**, *12*, 237–268.

[13] a) F. E. Osterloh, *J. Am. Chem. Soc.* **2002**, *124*, 6248–6249; b) J. Y. Kim, H. Hiramatsu, F. E. Osterloh, *J. Am. Chem. Soc.*

2005, *127*, 15556 – 15561; c) J. Y. Kim, F. E. Osterloh, *J. Am. Chem. Soc.* **2006**, *128*, 3868 – 3869.
[14] a) H. Hata, S. Kubo, Y. Kobayashi, T. E. Mallouk, *J. Am. Chem. Soc.* **2007**, *129*, 3064 – 3065; b) H. Hata, Y. Kobayashi, M. Salama, R. Malek, T. E. Mallouk, *Chem. Mater.* **2007**, *19*, 6588 – 6596.
[15] a) M. Wiegel, M. H. J. Emond, E. R. Stobbe, G. Blasse, *J. Phys. Chem. Solids* **1994**, *55*, 773 – 778; b) G. Blasse, L. G. J. de Haart, *Mater. Chem. Phys.* **1986**, *14*, 481 – 484.
[16] a) J.-M. Jehng, I. E. Wachs, *Chem. Mater.* **1991**, *3*, 100 – 107; b) S.-H. Byeon, H.-J. Nam, *Chem. Mater.* **2000**, *12*, 1771 – 1778.
[17] R. D. Shannon, *Acta Crystallogr. Sect. A* **1976**, *32*, 751 – 767.
[18] D. E. Scaife, *Solar Energy* **1980**, *25*, 41 – 54.
[19] W. J. Youngblood, S.-H. A. Lee, K. Maeda, T. E. Mallouk, *Acc. Chem. Res.* **2009**, *42*, 1966 – 1973.

